

Article

Hybrid Cathodes Composed of $K_3V_2(PO_4)_3$ and Carbon Materials with Boosted Charge Transfer for K-Ion Batteries

Xianghua Zhang ¹, Xinyi Kuang ¹, Hanwen Zhu ¹, Ni Xiao ², Qi Zhang ¹, Xianhong Rui ^{1,3,*}, Yan Yu ^{3,4,5,*} and Shaoming Huang ^{1,*}

¹ Guangzhou Key Laboratory of Low-Dimensional Materials and Energy Storage Devices, Collaborative Innovation Center of Advanced Energy Materials, School of Materials and Energy, Guangdong University of Technology, Guangzhou 510006, China; xhzhang@mail2.gdut.edu.cn (X.Z.); kxinyi@126.com (X.K.); zhu975181134@163.com (H.Z.); qzhangmse@gdut.edu.cn (Q.Z.)

² Aviation Fuel Research & Development Center, China National Aviation Fuel Group Limited, Beijing 102603, China; xiaoni@cnafl.com

³ Hefei National Laboratory for Physical Sciences at the Microscale, Department of Materials Science and Engineering, CAS Key Laboratory of Materials for Energy Conversion, University of Science and Technology of China, Hefei 230026, China

⁴ Dalian National Laboratory for Clean Energy (DNL), Chinese Academy of Sciences, Dalian 116023, China

⁵ State Key Laboratory of Fire Science, University of Science and Technology of China, Hefei 230026, China

* Correspondence: xrui@gdut.edu.cn (X.R.); yanyumse@ustc.edu.cn (Y.Y.); smhuang@gdut.edu.cn (S.H.)

Received: 3 December 2019; Accepted: 10 January 2020; Published: 11 January 2020



Abstract: K-ion batteries (KIBs) have emerged as an auspicious alternative to Li-ion batteries (LIBs) owing to their uniform distribution, plentiful reserves, the low cost of K resources, and their similar physicochemical properties to Li resources. The development of KIBs is seriously limited by cathode materials. Here, a hybrid of $K_3V_2(PO_4)_3$ (KVP) particles triple-coated by amorphous carbon, carbon nanotubes (CNTs), and reduced graphene oxide (rGO) nanosheets (KVP/C/CNT/rGO) was fabricated by a facile ball milling process followed by heat treatment. Consequently, a stable capacity of 57 mAh g⁻¹ can be achieved at 0.2C, and a slow capacity decaying rate (0.06% per cycle) is displayed during 500 cycles under a high current density of 5C. The remarkable reversible capacity and excellent long-term cycling life are mainly due to the enhanced interwoven C/CNT/rGO networks and superior KVP crystal structure stability, which can provide multi-channel for fast electron transport and effective K⁺ diffusion.

Keywords: K-ion batteries; $K_3V_2(PO_4)_3$; boosted charge transfer; high rate; cycling stability

1. Introduction

Currently, the requirement for energy storage devices (e.g., Li-ion batteries (LIBs)) is increasing rapidly with the fast development of electric vehicles [1–3]. Yet, new concerns have been activated that the widespread use of LIBs may not satisfy the large-scale demand tomorrow because of uneven distribution, limited reserves, and the increasing cost of lithium minerals [4–9]. Many efforts have been made to exploring standout alternatives to LIBs. Rechargeable K-ion batteries (KIBs) have provoked tremendous interest due to the similar physical and chemical characters to Li and the abundant reserves of K resources [10–12]. Meanwhile, standard electrode potential of potassium (−2.94 V vs. E°) is close to that of lithium (−3.04 V vs. E°), indicating comparable working voltage for KIBs [13–15]. Moreover, due to weak Lewis acidity of K⁺, the corresponding Stoke's radius in liquid electrolyte is relatively small, making K⁺ possesses more excellent mobility than that of Li⁺ and Na⁺, and a better

rate performance for KIBs [16–18]. Therefore, tremendous diligence has been dedicated to the advance of superior KIBs with high energy density and rate performance.

Recently, anode materials, such as carbon materials (e.g., graphite [17,19] and KC_8 [20]), titanates (e.g., $K_2Ti_8O_{17}$ [16,21]), Sn-based hybrids, (e.g., Sn–C [22]), and P-based compounds (e.g., Sn_4P_3 [23], black phosphorus [24], etc.), were explored in depth and showed superior electrochemical properties for KIBs. However, relatively few cathode materials are known to be available for KIBs.

Potassium vanadium phosphate, $K_3V_2(PO_4)_3$ (KVP), has aroused wide interest since the successful application of congeneric $Li_3V_2(PO_4)_3$ and $Na_3V_2(PO_4)_3$ cathodes in LIBs and sodium ion batteries (SIBs) respectively [25–28]. This is mainly due to the high electrochemical activity of multiple variable vanadium valences, high redox potential, and excellent thermal stability caused by the induction effect of PO_4^{3-} [29–31]. Unfortunately, phosphate lacks good electronic conductivity, leading to unsatisfying rate capacity and cycle performance. Conventionally, the most common and simple modification strategy is to wrap the crystal particles with a conductive carbon layer (e.g., amorphous carbon [32–34]). For example, Xu et al. explored a three-dimensional KVP/C nanocomposite which exhibited a high-potential platform (3.6–3.9 V), but suffered from a poor rate capability (maximum current density: 200 mA g^{-1}) [30]. Another related work was the KVP/C composite synthesized by Liu's group, which exhibited relatively low capacity (e.g., only 31 mAh g^{-1} at 15 mA g^{-1}) [35]. Their inferior KIBs performance may arise from large KVP particles (micron scale) and unsatisfactory carbon coating with some bare regions. Therefore, it is necessary to downsize KVP particles and completely embed them into a conductive carbon network as high-performance cathode materials for KIBs.

In this work, to boost effective charge transfer, a hybrid cathode composed of KVP nanoparticles embedded in amorphous carbon, carbon nanotubes (CNTs), and reduced graphene oxide (rGO) nanosheets (denoted as KVP/C/CNT/rGO) was proposed for fabrication. The triple carbon materials can provide integrated electron transfer pathways throughout the whole electrode and suppress the strain produced during repeated potassium insertion/extraction. As a result, the KVP/C/CNT/rGO composite could deliver remarkable rate capability as well as excellent cycling performance (e.g., showing capacity retention of 86% after 500 cycles at 5C).

2. Materials and Methods

2.1. Synthesis of KVP-Based Composites

The raw materials (NH_4VO_3 , KH_2PO_4 and $C_6H_8O_7$) were purchased from Shanghai Sigma Chemical Reagent Co., Ltd., Shanghai, China. The commercial CNTs (XFM34) was bought from Nanjing XFNANO Materials Tech Co., Ltd., Nanjing, China. The commercially available rGO nanosheets (SE1233) were obtained from Changzhou Sixth Element Materials Technology Co., Ltd., Changzhou, China. All chemicals were used without any pretreatment. The KVP/C/CNT/rGO composite was fabricated by a simple ball milling process followed by a calcination step. Firstly, 2 mmol NH_4VO_3 and 3 mmol KH_2PO_4 were mixed and then an appropriate amount of $C_6H_8O_7$, CNTs, and rGO nanosheets were added sequentially (the mass ratio of KVP/ $C_6H_8O_7$ /CNTs/rGO = 1:0.3:0.3:0.3). Then, the mixture was put in agate containers containing 50 mL ethanol to conduct planetary ball milling (PMQW2, rotation rate: 350 rpm) for 24 h. Subsequently, the mixture solution was transferred into a beaker and dried at $70 \text{ }^\circ\text{C}$ in an oven to evaporate ethanol. Finally, the ball-milled precursor was preheated at $350 \text{ }^\circ\text{C}$ for 4 h and then annealed at $750 \text{ }^\circ\text{C}$ (heating rate: $5 \text{ }^\circ\text{C min}^{-1}$) for 12 h in Ar/ H_2 atmosphere. For comparison, based on the same method, reference samples with the addition of only one carbon source (the mass ratio of KVP/carbon source = 1:0.9) were also prepared, and the samples obtained from the carbon sources of $C_6H_8O_7$, CNTs, and rGO nanosheets were marked as KVP/C, KVP/CNT, and KVP/rGO, respectively.

2.2. Materials Characterization

The X-ray diffractometer (XRD, Rigaku D/max 2500, Rigaku, Tokyo, Japan) was employed to record the XRD patterns of the obtained samples with a Cu K α X-ray source scanned in the 2θ range of 5–60°. Raman spectra were carried out on the LabRAM HR Evolution with a laser wavelength of 532 nm. Thermogravimetric analysis (TGA, DSC3+, Switzerland) was conducted in air atmosphere from ambient temperature to 800 °C (heating rate: 10 °C min⁻¹). Nitrogen adsorption/desorption isotherms were performed by an Automatic specific surface and porosity analyzer (ASAP 2460, Micromeritics, Norcross, PA, America). The morphology and microstructure of KVP-based composites were examined by field-emission scanning electron microscopy (FESEM, SU-8220, Hitach, Tokyo, Japan) and transmission electron microscopy (TEM, JEM-2100F, JEOL, Tokyo, Japan).

2.3. Electrochemical Measurements

The coin-type cells were assembled in the glovebox with Ar (H₂O < 0.1 ppm, O₂ < 0.1 ppm). The working electrode (i.e., cathode) was produced by dispersing 90 wt % KVP/C/CNT/rGO and 10 wt % poly(vinylidene fluoride) (PVDF) in a solvent of *N*-methylpyrrolidone (NMP) under vigorous stirring, and the as-obtained slurry was then coated on aluminum foils. The anode was potassium foil, and the electrolyte contains 0.8 M KPF₆ in mixed solvent of propylene carbonate (PC) and ethylene carbon (EC). Afterwards, they were assembled in coin-type cells, and the corresponding electrochemical performance was evaluated on a NEWARE battery system. The cyclic voltammogram (CV) curves and electrochemical impedance spectra (EIS) were executed on an electrochemical workstation (Multi-Autolab M204, Metrohm, Kanaalweg, Netherlands).

3. Results and Discussions

Figure 1a demonstrates the X-ray diffraction (XRD) pattern of the as-synthesized KVP/C/CNT/rGO composite. The diffraction peaks are consistent with the previously reported results in the literature [30,36], which indicate successful formation of highly crystalline K₃V₂(PO₄)₃ phase. The Raman spectrum is displayed in Figure 1b. The two broad bands observed at around 1343 and 1581 cm⁻¹ correspond to the D-band of disordered carbon and G-band of crystalline graphite, respectively [37]. The peak intensity ratio of these two bands (I_D/I_G) is 1.28. Thermogravimetry (TG) analysis was tested in an air atmosphere to ascertain the total amount of C/CNT/rGO in the composite. As shown in Figure 1c, large weight loss occurred from 300 to 580 °C, which is ascribed to flaming of carbon materials, and the corresponding amount was determined to be 35 wt %. The last part with a slight weight increase from 580 to 800 °C is due to the oxidation of V³⁺. Based on these, the content of carbon material in KVP/C/CNT/rGO composite was calculated to be 35 wt %. Nitrogen isothermal adsorption/desorption evaluation was performed to further characterize the surface area and porosity of KVP/C/CNT/rGO composite, displayed in Figure 1d. The surface area determined by Brunauer–Emmett–Teller (BET) method is 122.7 m² g⁻¹, and a pore size distribution of around 4 nm is displayed by the Barret–Joyner–Halenda (BJH) profile. It can be believed that a high surface area may furnish many active sites for electrochemical reactions, and the porous structure can promote ion transport.

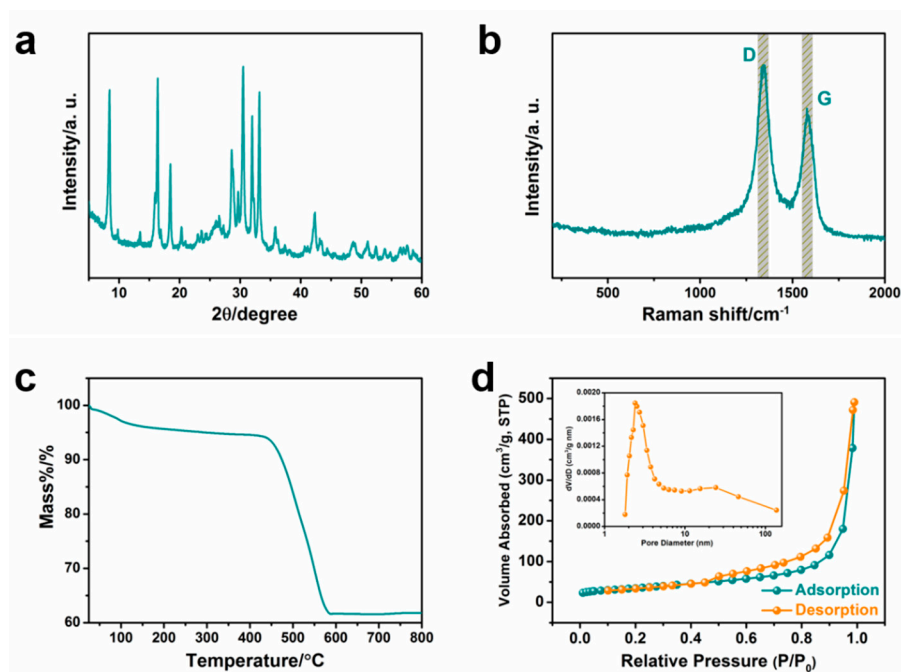


Figure 1. (a) XRD pattern; (b) Raman spectrum (D and G bands are marked by two shadow lines); (c) TGA curve; and (d) N₂ adsorption/desorption isotherms of the KVP/C/CNT/rGO composite (inset in (d): the pore size distribution profile of KVP/C/CNT/rGO derived from the desorption branch isotherm).

Figure 2a–e display FESEM and TEM images of the as-prepared KVP/C/CNT/rGO composite. It can be observed that KVP particles with diameters of 100–500 nm are embedded in the interwoven network of CNTs and rGO nanosheets. As seen from Figure 2g, high-resolution TEM (HRTEM) image reveals that KVP particles are coated by a layer of amorphous carbon (thickness: 5–10 nm), which can forcefully inhibit the particle growth at 750 °C and further promote the electronic conductivity. Moreover, elemental mapping performed by energy-dispersive X-ray analysis (Figure 2g) certifies the co-existence and uniform dispersion of C, K, V, P, and O in KVP/C/CNT/rGO composite.

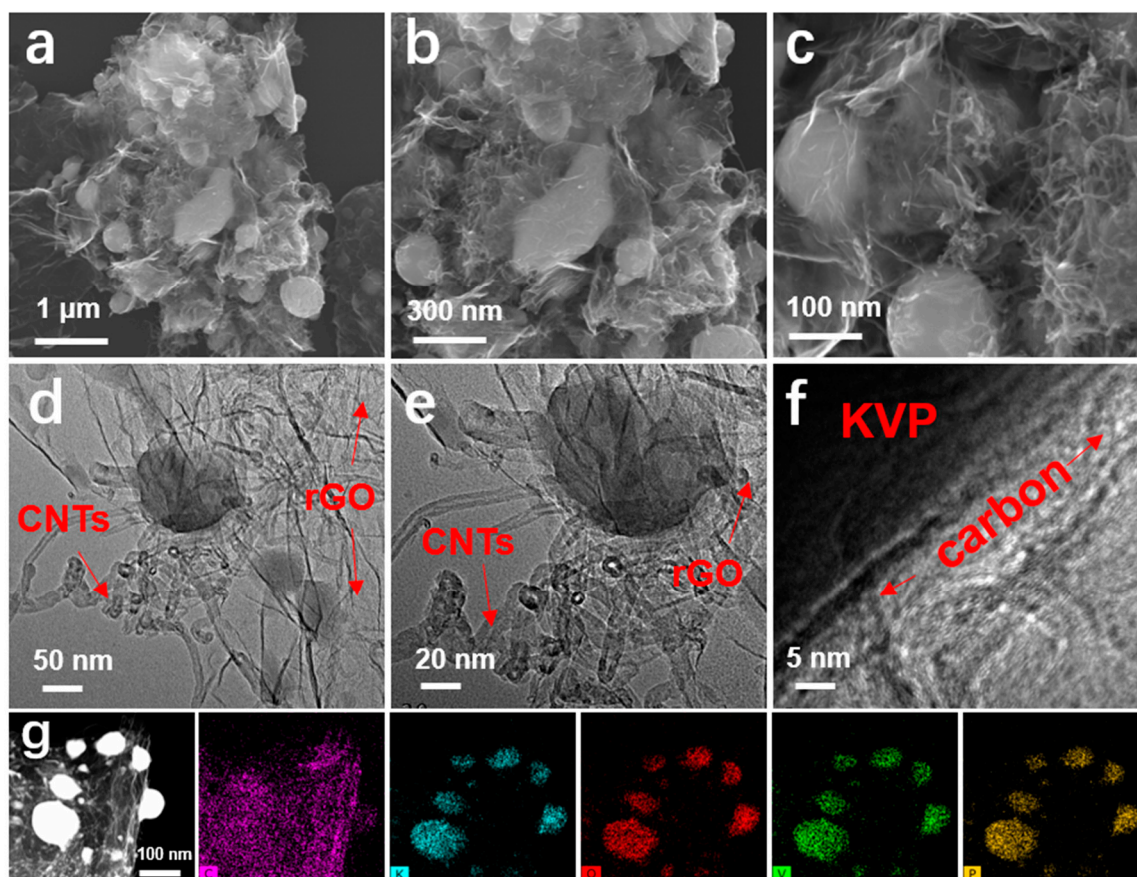


Figure 2. (a–c) SEM images; (d,e) TEM images; (f) HRTEM image; and (g) element (C, K, O, V and P) distribution mapping images of the as-obtained KVP/C/CNT/rGO composite.

Electrochemical behavior of KVP/C/CNT/rGO composite as KIBs cathode was evaluated between 2.5 and 4.3 V (vs. K^+/K). For comparison, three reference cathodes were also investigated, i.e., KVP/C, KVP/CNT, and KVP/rGO (the corresponding materials characterization shown in Supplementary Materials, Figures S1–S3). The charge and discharge profiles (the first five cycles) of the KVP/C/CNT/rGO composite at a low rate of 0.2C (here, 1C equals to 106 mA g^{-1} , assuming the full oxidation of vanadium ions from +3 to +4 [30]) are shown in Figure 3a. There are two charge (3.7 and 4.0 V) and discharge (3.5 and 3.8 V) plateaus, corresponding to reversible insertion and removal of potassium ions. The corresponding differential capacity curves display two pairs of reversible anodic/cathodic peaks (Figure 3b), further confirming two-phase transformation mechanisms. In addition, it is also noted that the redox peaks in cyclic voltammetric curves at 0.1 mV s^{-1} show good consistency with the above charge–discharge curves (Supplementary Materials, Figure S4). Such a cathode delivers relatively high initial charge (87 mAh g^{-1}) and discharge (57 mAh g^{-1}) capacities. By contrast, the other three KVP/rGO, KVP/CNT, and KVP/C cathodes show discharge capacities of only 37, 45, and 30 mAh g^{-1} , respectively (Supplementary Materials, Figure S5). Figure 3c shows the cycle performance (current density: 0.2C) of the KVP/C/CNT/rGO composite after activation for three cycles. It is found that this cathode exhibits a capacity retention of 86% (i.e., preserving reversible capacity of 49 mAh g^{-1}) after 200 cycles with the coulombic efficiency of approximately ~88%. By contrast, the control composites show obvious capacity losses and achieve discharge capacities of 31, 38, and 24 mA h g^{-1} (i.e., 82%, 84%, and 79% capacity retention) after 200 cycles for KVP/rGO, KVP/CNT, and KVP/C composites, respectively (Supplementary Materials, Figure S6).

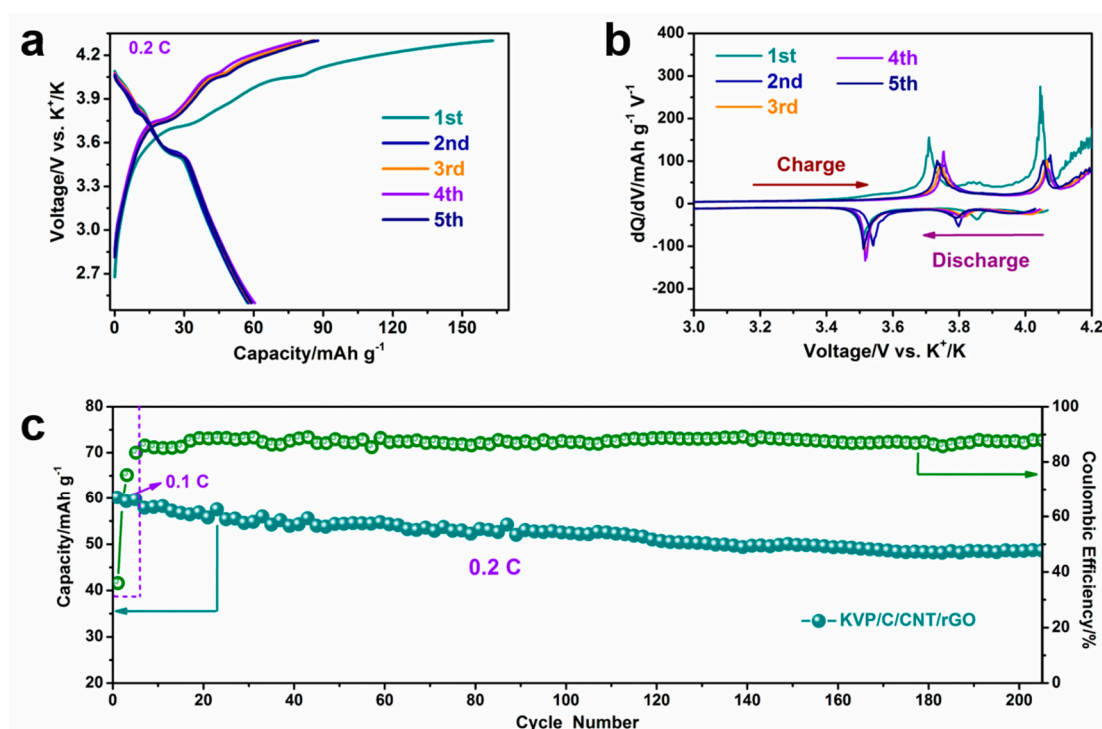


Figure 3. (a) Typical charge–discharge curves of the KVP/C/CNT/rGO composite at 0.2C; (b) The corresponding differential capacity plots; (c) Cycling capability for 200 cycles at 0.2C (green line: Coulombic efficiency).

Due to the attractive triple-modified multi-structure of the KVP/C/CNT/rGO composite, a remarkably superior rate performance was attained at various current rates from 0.2 to 5C. As seen from Figure 4a, it delivers satisfactory discharge capacities of 57, 50, 41, 30 and 20 mAh g⁻¹ at 0.2, 0.5, 1, 2, and 5C, respectively, and they can still reach 56 mAh g⁻¹ when the current returns to 0.2C. By contrast, the rate capabilities of the control samples are greatly inferior. For example, the KVP/rGO composite has discharge capacities of 20 and 12 mAh g⁻¹ when the rates are 2 and 5C respectively, and KVP/C only delivers 8 mAh g⁻¹ at 5C. On the other hand, the discharge capacity values of the KVP/C/CNT/rGO composite at different C rates are also superior to those of recently reported KVP/C cathodes of KIBs, e.g., 22 mAh g⁻¹ at 200 mA g⁻¹ (1.9C) for 3D KVP/C nanocomposites produced by Han et al. [30], and 31 mAh g⁻¹ at 15 mA g⁻¹ (0.14C) for carbon-coated KVP developed by Zhang et al. [35]. Figure 4b exhibits representative charge–discharge voltage plots of KVP/C/CNT/rGO composite at different rates. Obvious voltage platforms can be observed at low rates (e.g., 0.2–1C). With an increase in the rate, the voltage platforms become short but still visible, indicating that there is a slight polarization phenomenon in the high-rate cycling processes. Furthermore, the KVP/C/CNT/rGO composite also delivered an outstanding ultra-long high-rate (5C) cycling stability (Figure 4c). It is found that the initial specific capacity is about 20 mAh g⁻¹ (corresponding coulombic efficiency: 94%) and there is only about 0.06% capacity decaying per cycle within 500 charge–discharge processes.

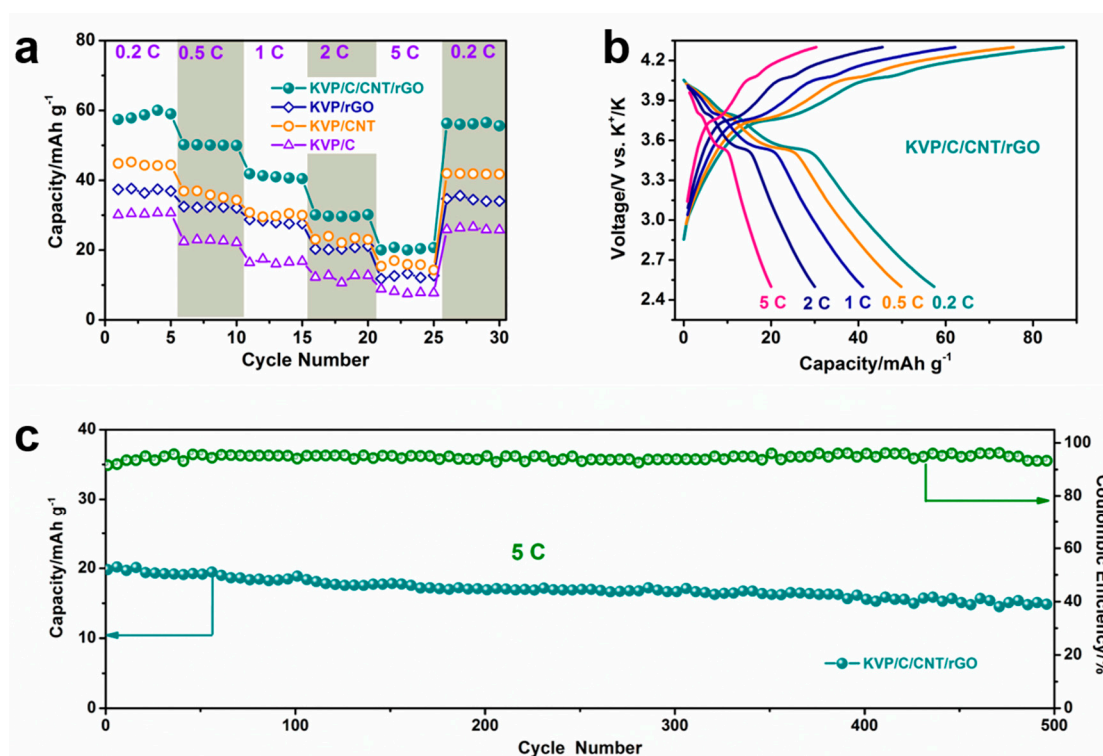


Figure 4. (a) Rate performance of KVP/C/CNT/rGO, KVP/rGO, KVP/CNT, and KVP/C from 0.2 to 5C; (b) Typical charge–discharge curves of the KVP/C/CNT/rGO composite from 0.2 to 5C; (c) Long-life cycling performance of the KVP/C/CNT/rGO composite at 5C (the cell was initially activated for three cycles at 0.1C, green line: Coulombic efficiency).

Figure 5a demonstrates the electrochemical impedance spectra (EIS) of KVP-based composites measured at the 10th full charged state. In the Nyquist plots, the semicircle (high-frequency range) represents the charge-transfer resistance (R_{ct}) occurring on the interface between electrode and electrolyte, and the sloped straight line (low-frequency range) corresponds to the K^+ diffusion resistance (Warburg resistance, W) [38,39]. The equivalent circuit model in Figure 5b is used to fit their kinetic behaviors. Consequently, the R_{ct} values of the KVP/C/CNT/rGO, KVP/rGO, KVP/CNT, and KVP/C are simulated to be about 98, 242, 304, and 371 Ω , respectively. The KVP/C/CNT/rGO with the lowest R_{ct} implies the fastest transfer kinetics for electron conduction and K^+ diffusion, which should be benefit from relatively small KVP particle size (shortening the lengths of solid-state K ion diffusion) and 3D interwoven C/CNT/rGO networks (facilitating fast electron transfer within the electrode and to the current collector).

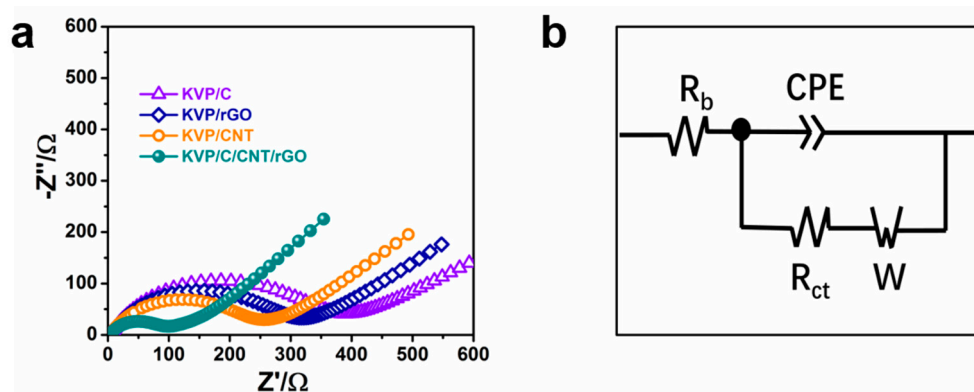


Figure 5. (a) The Nyquist plots of the KVP/C/CNT/rGO, KVP/rGO, KVP/CNT, and KVP/C composites; (b) The equivalent circuit model of the EIS measurement (R_b : ohmic resistance of solution and electrodes; CPE: double layer capacitance, R_{ct} : charge transfer resistance; W: Warburg impedance).

4. Conclusions

In summary, triple-coated KVP/C/CNT/rGO composite with superior electrochemical performance was synthesized by a convenient ball milling combined with high-temperature calcination process. The unique structure of the KVP/C/CNT/rGO composite—supported by amorphous carbon and CNTs as well as rGO nanosheets—provides hybrid ion/electron multichannel for fast electron transport and effective K^+ diffusion, improving the overall reaction kinetics. As a result, the KVP/C/CNT/rGO composite displays outstanding rate capability (e.g., 41 mAh g^{-1} (1C) and 20 mAh g^{-1} (5C)) and an excellent high-rate cycling performance, (e.g., about 0.06% capacity decaying per cycle during 500 cycles at 5C). We believe the superior electrochemical performance of KVP/C/CNT/rGO composite makes it an excellent cathode candidate superior to KIBs for energy storage applications.

Supplementary Materials: The following are available online at <http://www.mdpi.com/2571-9637/3/1/1/s1>. Figures S1–S3: materials characterization of KVP/C, KVP/CNT and KVP/rGO composites. Figure S4: CV curves of the KVP/C/CNT/rGO cathode at a scan rate of 0.1 mV s^{-1} . Figures S5 and S6: charge–discharge profiles and cycling performance of KVP/C, KVP/CNT and KVP/rGO at 0.2C.

Author Contributions: Conceptualization, X.R., Y.Y. and S.H.; methodology, X.R. and X.Z.; software, X.Z.; validation, X.Z., X.K. and H.Z.; investigation, X.Z., X.K., H.Z., Q.Z. and N.X.; data curation, X.R., X.Z., Q.Z. and N.X.; writing—original draft preparation, X.R. and X.Z.; writing—review and editing, X.R., Y.Y. and S.H.; funding acquisition, X.R., Y.Y. and S.H. All authors have read and agreed to the published version of the manuscript.

Funding: The authors gratefully acknowledge the National Key R&D Research Program of China (Grant No. 2018YFB0905400), National Natural Science Foundation of China (Grant Nos. 51802007, 51622210, 51872277, 21606003, 51972067, 51802044, 51672193, 51420105002 and 51920105004), Guangdong Natural Science Funds for Distinguished Young Scholar (Grant No. 2019B151502039), the DNL Cooperation Fund, CAS (DNL180310), the Fundamental Research Funds for the Central Universities (WK2060140026), and Opening Project of CAS Key Laboratory of Materials for Energy Conversion.

Conflicts of Interest: The authors declare no conflict of interest.

References

- Xu, B.; Qian, D.; Wang, Z.; Meng, Y.S. Recent progress in cathode materials research for advanced lithium ion batteries. *Mater. Sci. Eng. R Rep.* **2013**, *44*, 51–65. [[CrossRef](#)]
- Gao, M.R.; Xu, Y.F.; Jiang, J.; Yu, S.H. Nanostructured metal chalcogenides: Synthesis, modification, and applications in energy conversion and storage devices. *Chem. Soc. Rev.* **2013**, *42*, 2986–3017. [[CrossRef](#)]
- Chen, D.; Tan, H.T.; Rui, X.H.; Zhang, Q.; Feng, Y.Z.; Geng, H.B.; Li, C.C.; Huang, S.M.; Yu, Y. Oxyvanite V_3O_5 : A New Intercalation-Type Anode for Lithium-Ion Battery. *InfoMat* **2019**, *1*, 251–259.
- Rui, X.; Yan, Q.; Skyllas-Kazacos, M.; Lim, T.M. $Li_3V_2(PO_4)_3$ cathode materials for lithium-ion batteries: A review. *J. Power Sources* **2014**, *258*, 19–38. [[CrossRef](#)]

5. Chen, S.; Wu, C.; Shen, L.; Zhu, C.; Huang, Y.; Xi, K.; Maier, J.; Yu, Y. Challenges and Perspectives for NASICON-Type Electrode Materials for Advanced Sodium-Ion Batteries. *Adv. Mater.* **2017**, *29*, 1700431. [[CrossRef](#)]
6. Tan, H.; Chen, D.; Rui, X.; Yu, Y. Peering into Alloy Anodes for Sodium-Ion Batteries: Current Trends, Challenges, and Opportunities. *Adv. Funct. Mater.* **2019**, *29*, 1908745. [[CrossRef](#)]
7. Tan, H.; Xu, L.; Geng, H.; Rui, X.; Li, C.; Huang, S. Nanostructured $\text{Li}_3\text{V}_2(\text{PO}_4)_3$ Cathodes. *Small* **2018**, *14*, 1800567. [[CrossRef](#)]
8. Zhang, X.; Chen, D.; Liu, Y.; Han, W.; Chu, H.; Rui, X. Integrated Charge Transfer in $\text{Li}_3\text{V}_2(\text{PO}_4)_3/\text{C}$ for High-Power Li-Ion Batteries. *Int. J. Electrochem. Sci.* **2017**, *12*, 9925–9932. [[CrossRef](#)]
9. Chen, D.; Rui, X.; Zhang, Q.; Geng, H.; Gan, L.; Zhang, W.; Li, C.; Huang, S.; Yu, Y. Persistent zinc-ion storage in mass-produced V_2O_5 architectures. *Nano Energy* **2019**, *60*, 171–178. [[CrossRef](#)]
10. Hwang, J.Y.; Myung, S.T.; Sun, Y.K. Recent Progress in Rechargeable Potassium Batteries. *Adv. Funct. Mater.* **2018**, *28*, 1802938. [[CrossRef](#)]
11. Tan, H.; Feng, Y.; Rui, X.; Yu, Y.; Huang, S. Metal Chalcogenides: Paving the Way for High-Performance Sodium/Potassium-Ion Batteries. *Small Methods* **2019**, *10*, 1900563. [[CrossRef](#)]
12. Yang, D.; Liu, C.; Rui, X.; Yan, Q. Embracing high performance potassium-ion batteries with phosphorus-based electrodes: A review. *Nanoscale* **2019**, *11*, 15402–15417. [[CrossRef](#)] [[PubMed](#)]
13. Zhu, J.; Li, Y.; Yang, B.; Liu, L.; He, D. A Dual Carbon-based Potassium Dual Ion Battery with Robust Comprehensive Performance. *Small* **2018**, *14*, 1801836. [[CrossRef](#)] [[PubMed](#)]
14. Yu, Y.; Zhang, X.; Rui, X.; Chen, D.; Huang, S. $\text{Na}_3\text{V}_2(\text{PO}_4)_3$: An advanced cathode for sodium-ion batteries. *Nanoscale* **2019**, *11*, 2556–2576.
15. Kubota, K.; Dahbi, M.; Hosaka, T.; Kumakura, S.; Komaba, S. Towards K-Ion and Na-Ion Batteries as “Beyond Li-Ion”. *Chem. Rec.* **2018**, *18*, 459–479. [[CrossRef](#)]
16. Liao, J.; Hu, Q.; Che, B.; Ding, X.; Chen, F.; Chen, C. Competing with other polyanionic cathode materials for potassium-ion batteries via fine structure design: new layered KVOPO_4 with a tailored particle morphology. *J. Mater. Chem. A* **2019**, *7*, 15244–15251. [[CrossRef](#)]
17. Komaba, S.; Hasegawa, T.; Dahbi, M.; Kubota, K. Potassium intercalation into graphite to realize high-voltage/high-power potassium-ion batteries and potassium-ion capacitors. *Electrochem. Commun.* **2015**, *60*, 172–175. [[CrossRef](#)]
18. Zhang, X.; Yang, D.; Rui, X.; Yu, Y.; Huang, S. Advanced Cathodes for Potassium-Ion Battery. *Curr. Opin. Electrochem.* **2019**, *18*, 24–30. [[CrossRef](#)]
19. Jian, Z.; Luo, W.; Ji, X. Carbon Electrodes for K-Ion Batteries. *J. Am. Chem. Soc.* **2015**, *137*, 11566. [[CrossRef](#)]
20. Luo, W.; Wan, J.; Ozdemir, B.; Bao, W.; Chen, Y.; Dai, J.; Lin, H.; Xu, Y.; Gu, F.; Barone, V. Potassium Ion Batteries with Graphitic Materials. *Nano Lett.* **2015**, *15*, 7671–7677. [[CrossRef](#)]
21. Han, J.; Xu, M.; Niu, Y.; Li, G.N.; Wang, M.; Zhang, Y.; Jia, M.; Li, C.M. Exploration of $\text{K}_2\text{Ti}_8\text{O}_{17}$ as an anode material for potassium-ion batteries. *Chem. Commun.* **2016**, *52*, 11274–11276. [[CrossRef](#)] [[PubMed](#)]
22. Sultana, I.; Ramireddy, T.; Rahman, M.M.; Chen, Y.; Glushenkov, A.M. Tin-based composite anodes for potassium-ion batteries. *Chem. Commun.* **2016**, *52*, 9279–9282. [[CrossRef](#)] [[PubMed](#)]
23. Zhang, W.; Mao, J.; Li, S.; Chen, Z.; Guo, Z. Phosphorus-Based Alloy Materials for Advanced Potassium-Ion Battery Anode. *J. Am. Chem. Soc.* **2017**, *139*, 3316–3319. [[CrossRef](#)] [[PubMed](#)]
24. Sultana, I.; Rahman, M.M.; Ramireddy, T.; Ying, C.; Glushenkov, A.M. High capacity potassium-ion battery anodes based on black phosphorus. *J. Mater. Chem. A* **2017**, *5*, 23506–23512. [[CrossRef](#)]
25. Rui, X.; Sim, D.; Wong, K.; Zhu, J.; Liu, W.; Xu, C.; Tan, H.; Xiao, N.; Hng, H.H.; Lim, T.M. $\text{Li}_3\text{V}_2(\text{PO}_4)_3$ nanocrystals embedded in a nanoporous carbon matrix supported on reduced graphene oxide sheets: Binder-free and high rate cathode material for lithium-ion batteries. *J. Power Sources* **2012**, *214*, 171–177. [[CrossRef](#)]
26. Rui, X.; Li, C.; Chen, C. Synthesis and characterization of carbon-coated $\text{LiV}(\text{PO})$ cathode materials with different carbon sources. *Electrochim. Acta* **2009**, *54*, 3374–3380. [[CrossRef](#)]
27. Rui, X.; Li, C.; Liu, J.; Cheng, T.; Chen, C. The $\text{Li}_3\text{V}_2(\text{PO}_4)_3/\text{C}$ composites with high-rate capability prepared by a maltose-based sol–gel route. *Electrochim. Acta* **2010**, *55*, 6761–6767. [[CrossRef](#)]
28. Rui, X.; Sun, W.; Wu, C.; Yu, Y.; Yan, Q. An Advanced Sodium-Ion Battery Composed of Carbon Coated $\text{Na}_3\text{V}_2(\text{PO}_4)_3$ in a Porous Graphene Network. *Adv. Mater.* **2015**, *27*, 6670–6676. [[CrossRef](#)]

29. Hong, S.; Kim, Y.; Park, Y.; Choi, A.; Choi, N.S.; Lee, K.T. Charge Carriers in Rechargeable Batteries: Na Ions vs. Li Ions. *Energy Environ. Sci.* **2014**, *45*, 2067–2081. [[CrossRef](#)]
30. Han, J.; Li, G.; Liu, F.; Wang, M.Q.; Xu, M.W. Investigation of $K_3V_2(PO_4)_3/C$ nanocomposite as high-potential cathode materials for potassium-ion batteries. *Chem. Commun.* **2017**, *53*, 1805–1808. [[CrossRef](#)]
31. Liu, P.; Zhu, K.; Gao, Y.; Luo, H.; Li, L. Recent Progress in the Applications of Vanadium-Based Oxides on Energy Storage: From Low-Dimensional Nanomaterials Synthesis to 3D Micro/Nano-Structures and Free-Standing Electrodes Fabrication. *Adv. Energy Mater.* **2017**, *7*, 1700547.
32. Liu, T.; Bo, W.; Gu, X.; Lei, W.; Min, L.; Gao, L.; Wang, D.; Zhang, S. All-climate sodium ion batteries based on the NASICON electrode materials. *Nano Energy* **2016**, *30*, 756–761. [[CrossRef](#)]
33. Islam, S.; Alfaruqi, M.H.; Putro, D.Y.; Mathew, V.; Kim, J. Pyrosynthesis of $Na_3V_2(PO_4)_3@C$ Cathodes for Safe and Low-Cost Aqueous Hybrid Batteries. *Chemsuschem* **2018**, *11*, 2239–2247. [[CrossRef](#)] [[PubMed](#)]
34. Cao, J.; Wang, Y.; Wang, L.; Yu, F.; Ma, J. $Na_3V_2(PO_4)_3@C$ as Faradaic Electrodes in Capacitive Deionization for High-Performance Desalination. *Nano Lett.* **2019**, *19*, 823–828. [[CrossRef](#)] [[PubMed](#)]
35. Zhang, L.; Zhang, B.; Wang, C.; Dou, Y.; Zhang, Q.; Liu, Y.; Gao, H.; Al-Mamun, M.; Pang, W.K.; Guo, Z.; et al. Constructing the best symmetric full K-ion battery with the NASICON-type $K_3V_2(PO_4)_3$. *Nano Energy* **2019**, *60*, 432–439. [[CrossRef](#)]
36. Wang, X.; Niu, C.; Meng, J.; Ping, H.; Xu, X.; Wei, X.; Liang, Z.; Zhao, K.; Wen, L.; Yan, M. Novel $K_3V_2(PO_4)_3/C$ Bundled Nanowires as Superior Sodium-Ion Battery Electrode with Ultrahigh Cycling Stability. *Adv. Energy Mater.* **2015**, *5*, 1500716.
37. Rajagopalan, R.; Lei, Z.; Shi, X.D.; Hua, K.L. Tuned In Situ Growth of Nanolayered rGO on 3D $Na_3V_2(PO_4)_3$ Matrices: A Step toward Long Lasting, High Power Na-Ion Batteries. *Adv. Mater. Interfaces* **2016**, *3*, 1600007. [[CrossRef](#)]
38. Yu, J.; Zhou, X.; Li, D.; Cheng, X.; Liu, F.; Yan, Y. Highly Reversible Na Storage in $Na_3V_2(PO_4)_3$ by Optimizing Nanostructure and Rational Surface Engineering. *Adv. Energy Mater.* **2018**, *8*, 1800068.
39. Macfarlane, D.; Chinnareddy, M.V.; Mitra, S.; Forsyth, M.; Kar, M.; Raj, A.K. Stability enhancing ionic liquid hybrid electrolyte for NVP@C cathode based sodium batteries. *Sustain. Energy. Fuels* **2018**, *2*, 566–576.



© 2020 by the authors. Licensee MDPI, Basel, Switzerland. This article is an open access article distributed under the terms and conditions of the Creative Commons Attribution (CC BY) license (<http://creativecommons.org/licenses/by/4.0/>).